

1 Article

2 **Biological activity and nanostructuration of Fe₃O₄-Ag** 3 **/polyethylene nanocomposites**

4 **Phuong Nguyen-Tri**

5 ¹ Department of Chemistry, University of Montréal, Quebec, Canada;
6 Email: Phuong.nguyen.tri@umontreal.ca (P. Nguyen-Tri); Tel. + 514-340 5121 (7326):

7

8 **Abstract:** We report here the synthesis of uniform nanospheres-like silver nanoparticles (AgNPs, 5-
9 10 nm) and the dumbbell-like Fe₃O₄-Ag hybrid nanoparticles (FeAgNPs, 8-16 nm) by the use of
10 seeding growth method in the presence of oleic acid (OA)/ oleylamine (OLA) as surfactants. The
11 antibacterial activity of pure nanoparticles and nanocomposites by monitoring the bacterial lag–log
12 growth has been investigated. The electron transfer from AgNPs to Fe₃O₄NPs which enhances the
13 biological of silver nanoparticles has been proven by nanoscale Raman spectroscopy. The lamellae
14 structure in the spherulite of FeAgNPs/PE nanocomposites seems play the key role to the
15 antibacterial activity of nanocomposites, which has been proven by nanoscale AFM-IR. An atomic
16 force microscopy coupled with nanoscale infrared microscopy (AFM-IR) is use to highlight the
17 distribution of nanoparticles on the surface of nanocomposite at the nanoscale. The presence of
18 FeAgNPs in PE nanocomposites has a better antibacterial activity than that reinforced by AgNPs
19 due to the faster Ag⁺ release rate from the Fe₃O₄-Ag hybrid nanoparticles and the ionization of
20 AgNPs in hybrid nanostructure.

21 **Keywords:** Polyethylene, nanocomposites, silver nanoparticles, Fe₃O₄-Ag hybrid nanoparticles,
22 antibacterial activity
23

24 1. Introduction

25 The transmission of infectious diseases by bacteria in in airports, hospitals and other public
26 places is increasing in the last few decades¹. The development of self-sterilizing polymers²⁻³ able to
27 inactivate bacteria loaded with antibacterial agents is a way to increase the bactericide performance
28 of surfaces designed to disinfect spaces spreading the infections due to toxic biofilms. *E. coli* has been
29 reported to lead food poisoning⁴⁻⁵. Silver nanoparticles are reported to be effective biocidal agents
30 against various bacteria⁶⁻⁹. The recent report approved that the antibacterial activity comes from silver
31 ions (Ag⁺), not from Ag metallic⁶. Different components are combined with silver to yield a
32 nanoentity with desired properties not afforded by their counterparts. For example, combination of
33 Ferrite and silver is expected to enhance the antibacterial activity due to the electron transfer between
34 two these metals and thus enhances the release of silver ions, the main against for the inactivation of
35 bacteria and virus. The magnetic properties of ferrite leads to the formation of superparamagnetic
36 composites which are useful in carcinoembryonic antigen in clinical immunoassay¹⁰ and water
37 treatment due to its enable easy separation from solution¹¹.

38 The biological activity of silver can be enhanced in combination with other transition metals
39 such as nano-silver-ferrite composite¹² The highest antibacterial effect of 99.4% was achieved at 5.4
40 wt % of NPs and the driving frequency of 100 rpm. A time-dependent antibacterial effect in 0.1 wt %
41 of Ag/Fe₃O₄ was also observed which indicated that the use of specific rotating magnetic fields to
42 manipulate Ag/Fe₃O₄ magnetic NPs can significantly improve the antibacterial efficacy to *E. coli* and
43 the highest antibacterial effect can be achieved to 99.4%. The antibacterial silk from Fe₃O₄-Ag have
44 with have high antibacterial activities against both *Escherichia coli* and *Staphylococcus aureus* been
45 also synthesized¹³. The author confirmed that the as prepared antibacterial silks be easily recycled

46 without a decrease in their antibacterial activities due to the synergistic effects between the Ag NPs
47 and Fe₃O₄ NPs with large amounts of active sites¹³. Depending on synthesis conditions, various
48 morphologies of hybrid nanoparticles can be achieved¹⁴⁻¹⁶.

49 Polyolefin (PP and PE) remains the most consumed polymer in the world due to its interesting
50 good mechanical properties, its stability and its low cost^{14, 17-22}. The addition of additive brings this
51 polymer various new properties depending on end-end applications²³⁻²⁵. Here, the main goal of this
52 work is to prepare of the hybrid silver nanoparticles with high antibacterial activity and then
53 incorporated in the polyethylene matrix and investigate its antibacterial activity. Some recent pointed
54 techniques such as atomic force microscopy coupled with nanoscale infrared (AFM-IR) and nanoscale
55 Raman (AFM-Raman) will be used for better understanding the release behavior on the composite
56 surfaces and propose the possible mechanism for the enhancement of the antibacterial activity.

57 The atomic force microscope (AFM) has been widely used for the study of nanocomposites and
58 polymeric materials with nanoscale spatial resolution²⁶⁻³³. AFM-IR allows surface mapping with a
59 resolution of several tens of nanometers. The main limitation of AFM-IR concerns the laser source
60 near infrared (900-4000 cm⁻¹) region. Detection of the bonding signals between polymer and metals
61 appearing below 900 cm⁻¹ cannot be detected. The nano-Raman can overcome these drawbacks. AFM-
62 Raman combines confocal Raman spectroscopy and imaging providing specific chemical information
63 on the nano-materials with a sub-micron spatial resolution³⁴⁻³⁷.

64 We show in this study that AFM-IR and AFM-Raman can be used to investigate the nanoscale
65 structure and the electron transfer in hybrid nanoparticles. The detailed microstructure of FeAgNP
66 and PE nanocomposites containing Fe₃O₄-Ag hybrid nanoparticles is addressed in this study. The
67 release mechanism was investigated when these nanoparticles were incorporated in PE. The effect of
68 these nanoparticles on the lamellae structure of PE was also worked out in the course of this study.

69 2. Materials and Methods

70 2.1. Chemicals

71 Iron(III) acetylacetonate (Fe(acac)₃) 99.99 %; silver nitrate (AgNO₃) 99 %; sodium borohydride
72 (NaBH₄) 99 % and sodium stearate 99 %; solvents: 1-octadecene, di-chlorobenzene (DCB, 99 %),
73 absolute ethanol and hexane; surfactants and reductant: oleic acid (OA) 99 %, oleylamine (OLA) 70
74 %, 1,2 n-hexadecanediol (HDD) 90 %, polyvinylpyrrolidone (PVP) were purchased from Sigma-
75 Aldrich. HDPE granules were purchased from IRPC Public Company (grade G2855 – Polimaxx
76 Polene, Thailand).

77 2.2. Synthesis of nanoparticles

78 AgNPs were prepared by the reduction of silver nitrate using sodium borohydride in the
79 presence of PVP in distilled water. A 20 mL volume of 5 mM silver nitrate was added dropwise to
80 200 mM of PVP (at 0.1 wt.%), then 50 mL of 10 mM chilled sodium borohydride solution was added
81 drop-wise into the above mixture. The reaction mixture was stirred vigorously during 30 min by
82 using a magnetic stirring plate and sonicated for another 30 min. Afterwards, the AgNPs was
83 extracted with 100 mL xylene at 50 °C.

84 Synthesis of Fe₃O₄ nanoparticles: the Fe₃O₄ nanoparticles (Fe₃O₄ NPs) were prepared by
85 pouring cetylacetonate (0.162 g, 0.63 mM), Fe (III) acetylacetonate (0.6 g, 1.9 mM) and hexadecanediol
86 (0.58 g, 1.5 mM) into a 100 mL three-neck flask. At the same time, 3.6 mL OA, 3.6 mL OLA and 30 mL
87 1-octadecene were added into the above mixture. The concentrations of Fe(acac)₃, OA, OLA, and
88 HDD in the solution were equal to 63, 372, 372 and 75 mM, respectively. The reaction mixture was
89 stirred and degassed at room temperature for 30 min before heating to 100 °C, and kept at this
90 temperature for 30 min to remove water. The temperature was increased to 200 °C, and kept for 30
91 min. Then, the reaction solution was heated further to 295 °C at a heating rate of 5-7 °C/min and
92 maintained for 30 min before cooling to room temperature. The Fe₃O₄ NPs were then purified from
93 the excess ligands before the synthesis of Fe₃O₄-Ag as follows: 20 mL of the Fe₃O₄ NPs solution was
94 mixed with 20 mL of ethanol. The Fe₃O₄ NPs were then collected using a magnetic bar and the

95 supernatant was discarded. The Fe₃O₄ NPs were thereafter dispersed in 5 mL hexane and
96 precipitated by adding 5 mL of ethanol. The precipitation/re-dispersion procedure was repeated two
97 more times and the Fe₃O₄ NPs were finally dispersed in DCB.

98 Synthesis of Fe₃O₄-Ag hybrid nanoparticles: The seeding growth method was used to prepare
99 Fe₃O₄-Ag NPs. About 5 mL of DCB solution containing 500 mg AgNO₃ and 3 mL OLA was added
100 drop-wise into 20 mL DCB containing 100 mg purified Fe₃O₄ NPs (at 170 °C). The mixture was
101 maintained at this temperature for 60 min before cooling to room temperature.

102 2.3. Preparation of nanocomposites

103 The master batch of PE nanocomposites containing a high concentration of nanoparticles (2 wt.
104 %) was prepared by the mixing method. PE granules were dissolved in toluene (5 wt. %, stirring at
105 85 °C). The nanoparticles were then added to this solution following a sonication during 1h. Toluene
106 was then removed at (110 °C) under vacuum. To fabricate the final PE nanocomposite sheets, the
107 above as-prepared master batch was mixed with PE granules, and then blended in an internal
108 HAAKE mixer at 50 rpm and 170 °C for 8 min to extrude the final PE nanocomposites containing 0.1
109 wt. % of AgNPs.

110 To characterize the polymer nanostructure, a solution of 20 mg/ml was added in 1,2
111 dichlorobenzene and stirring during 24h, then heated up to 90 °C in the dark before casting it over
112 Si-wafer or gold substrates. Polymer films were dried under vacuum at 60 °C for 2 h to ensure
113 complete removal of residual solvent. The polymer film was then melted at 180 °C during 3 min to
114 ensure transformation to crystalline crystals and subsequently quenched to the selected
115 crystallization temperature at a cooling rate of 100 °C/min.

116 2.4. AFM-IR

117 The AFM-IR measurements were carried on a Nano-IR2 system (Anasys Instruments, CA, USA).
118 The AFM images were recorded in contact mode at a rate line 0.1-1 Hz using a gold-plated silicon
119 nitride probe (Anasys Instruments, CA, USA) with an elastic constant of about 0.5 N.m⁻¹ and nominal
120 radius of 10 nm. The nanoscale IR spectra were collected directly on the single fiber surface, deposited
121 on double-side adhesive tape within the 900-3600 cm⁻¹ range at a spectral resolution of 4 cm⁻¹, 256
122 co-averages. The single IR radiation image is recorded with a scan rate of 0.1 Hz, resolution 1024 x
123 1024 pixels and 16 co-averages, at a power limit within 0.5-4 % at a frequency of 196 Hz. All
124 measurements were carried out at room temperature in a room provided with humidity controller
125 (about 20 % RH). This precludes the effect of water absorption on the sample surface during the
126 analyzing. The nano-IR devices were located in an anti-vibration system.

127 2.5. AFM-Raman

128 The Raman spectra and AFM images were recorded on a Witec Alpha300 RSA unit equipped
129 with an AFM & SNOM Confocal Raman Microscope. The AFM images were recorded in contact
130 mode with a rate of 0.3 Hz using an AFM tip TESPA (Bruker, CA, USA). For nano-Raman spectra
131 measurements, the integration time was about 1s with 10 scans at a spectral resolution of 1 cm⁻¹ and
132 laser wavelength of 532 nm. The laser power was set at 15 mW to avoid sample burning.

133 2.6. UV-Vis analysis

134 An UV-Vis spectrophotometer, model CINTRA 4040 (GBC, USA) with 2 nm slit width was used
135 to monitor the absorbance of the chromophores and the electron transfer in the nanocomposites.

136 2.7. Antibacterial growth test

137 *E. coli* DH5 α bacteria were purchased from Invitrogen (USA). Luria- Broth medium was
138 provided by Merck (Germany). To evaluate the cell density, a Beckman Coulter DU-730 (USA) was
139 used. In this test, the optical density OD₆₀₀ measures the light absorbance of the *E. coli* sample.
140 Different cell strains may have different cell numbers at a given OD₆₀₀ value, but OD₆₀₀ = 1 usually

141 means that there are about 1×10^9 cells per ml culture. Bacterial pre-cultures were prepared to generate
142 subcultures of bacterial in the lag phase so that the number of bacterial cells was constant before the
143 log phase or exponential growth phase. In this way, the growth rate of the bacteria on the
144 nanocomposites was evaluated. The OD600 values in the range 0.1–2.0 for cell densities of *E. coli*
145 culture indicated the bacterial growth rates.

146 A volume of 100 μL of stock culture of *E. coli* in glycerol was pipetted into 3 mL of medium in a
147 15 mL test tube and shaken overnight at 200 rpm and 37 °C. Afterward, a 500 μL aliquot of pre-culture
148 was inoculated into 100 mL of medium in a 500 mL Erlenmeyer flask and shaken at 200 rpm and 37
149 °C until the OD600 absorbance value reached 0.3. These pre-cultures were used to account for the
150 bacterial growth rate.

151 The as-prepared nanocomposites were cut into 10×10 mm square samples and then washed with
152 acetone to remove all impurities on the sample surface and autoclaved at 130 °C for 20 min before
153 every test.

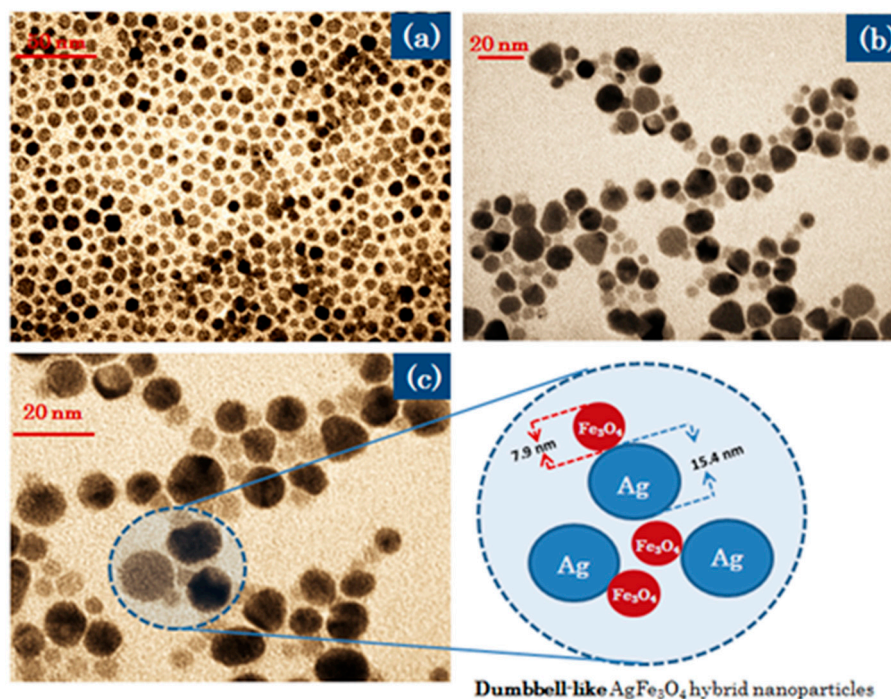
154 The monitoring test for the evaluation of the bacterial growth was adapted from procedures
155 described in the ASTM E 2149-10 standard. Ten square samples of autoclaved nanocomposites were
156 placed into each 100 mL bacterial pre-culture in a 500 mL Erlenmeyer flask (as described previously)
157 in which the OD600 had reached 0.3 and shaking was continued at 200 rpm at 37 °C. Then, the OD600
158 values of the bacterial cultures were monitored every 30 min until OD reached 2.0. The reported data
159 was the average of three cultures. The relative OD600 values were then standardized to evaluate the
160 effect of the nanocomposites on the growth rate of the bacteria. The pure bacterial cultures were used
161 as controls.

162 3. Results and discussion

163 3.1. Characterization of nanoparticles

164 Figure 1 shows the TEM images of $\text{Fe}_3\text{O}_4\text{NPs}$ (Fig. 1a), FeAgNPs (Fig. 1b and 1c) dispersed in an
165 organic solvent (DCB). Figure 1a shows the uniform particle distribution with a diameter of 6-8 nm.
166 Figure 1c shows that hybrid FeAgNPs with a uniform dumbbell-like structure: the bigger
167 nanoparticles are AgNPs and the smaller ones are $\text{Fe}_3\text{O}_4\text{NPs}$. It has to be noted that, the synthesis
168 process of hybrid nanoparticles was optimized to attain the reported sizes of the hybrid
169 nanoparticles.

170 The $\text{Fe}_3\text{O}_4\text{NPs}$ were synthesized and used as the seeding components before hybridization with
171 AgNPs; the average size of $\text{Fe}_3\text{O}_4\text{NPs}$ (about 6-8 nm) was not affected during the hybridization
172 process with AgNPs. Bigger sizes of AgNPs with an average about 15-16 nm were expected. During
173 the breeding processes both the temperature (170 °C) and an Ag-salt concentration 10 times higher
174 than the volume of Fe_3O_4 nanoparticles. The synthesis of dumbbell Ag- Fe_3O_4 hybrid systems with an
175 AgNPs size of about of 15-16 nm may be used as template to fabricate Au (hollow)- Fe_3O_4 in which a
176 plasmon-resonance peak in the near infrared region could be of interest for novel optical imaging
177 applications.



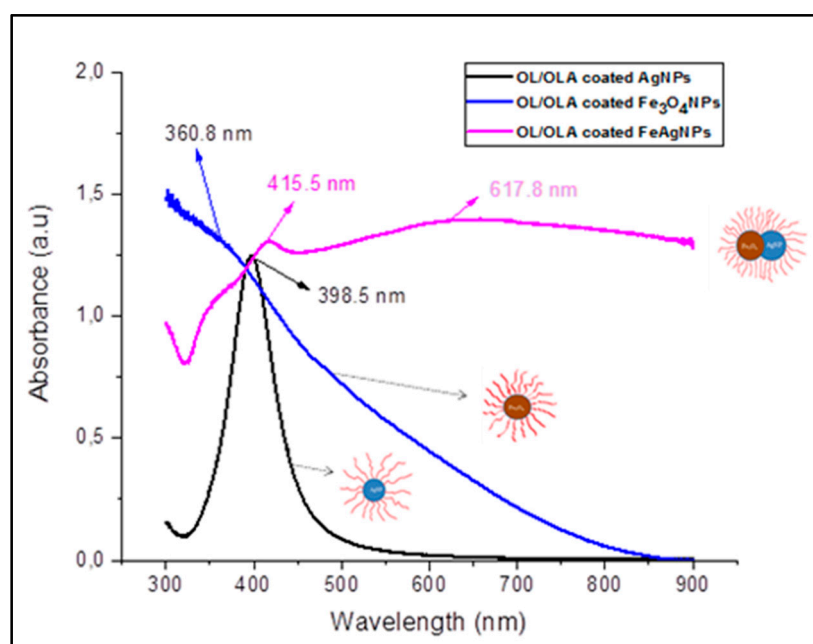
178

179

Figure 1. TEM images of OL/OLA coated Fe₃O₄NPs (a) and FeAgNPs (b, c) dispersed in DBC.

180 UV-Vis spectra of OL/OLA coated Fe₃O₄ NPs, AgNPs and FeAgNPs were carried out and the
 181 results are shown in Figure 2. A broad absorption band in the region of 300–600 nm for Fe₃O₄NPs
 182 was observed,³⁸ the shoulder at ~360.8 nm was due to nanosized Fe₃O₄NPs.³⁹ The band around 400
 183 nm is characteristic for the surface Plasmon resonance (SPR) peak of AgNPs⁴⁰.

184 The hybridization of AgNPs and Fe₃O₄NPs leads to a red shift in the SPR spectra and a significant
 185 broadening of the SPR peak. AgNPs, SPR peak is located at 398.5 nm, and at 415.5 nm for the Fe₃O₄-
 186 Ag hybrids. This red shift is assigned to the electron transfer between both samples leading to a
 187 depletion of the free electron density in the surface layer due to the increase of π back bonding with
 188 the ligand.⁴¹⁻⁴² In contrast, the presence of electron donors induces a blue-shift of SPR.⁴³⁻⁴⁴ The
 189 contribution of Fe₃O₄NPs nanoparticles gives raise to a band at ~360 nm. The peak at 617.8 nm could
 190 be assigned to the hybridization of AgNPs and Fe₃O₄ NPs.

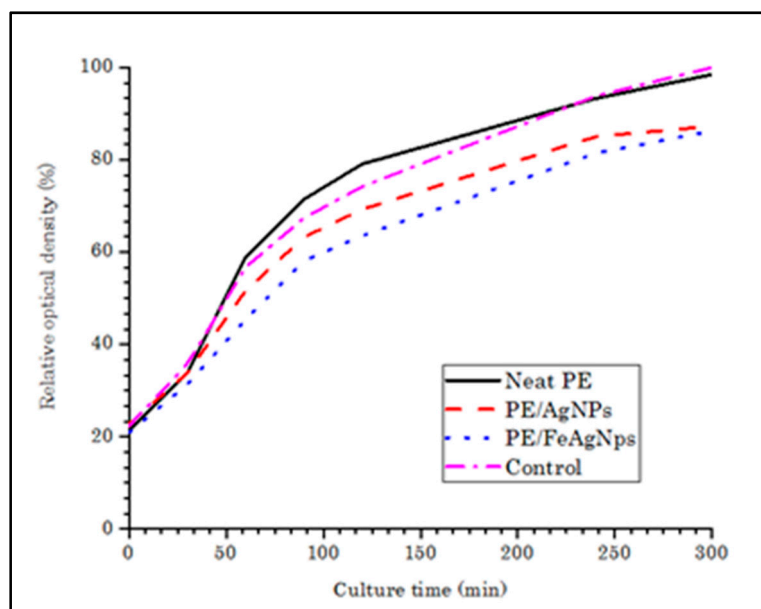


191

192 *Figure 2.* UV-visible absorption spectra of the OL/OLA coated Fe₃O₄ NPs, PVP coated AgNPs and
 193 OL/OLA coated FeAgNPs hybrid nanoparticles dispersed in hexane.

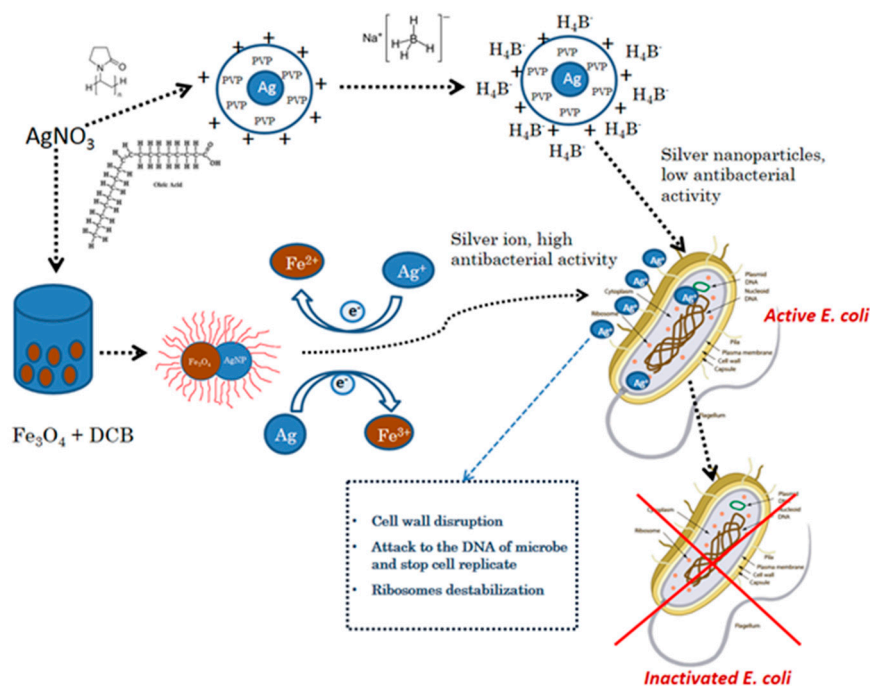
194 3.2. Antibacterial behavior of HDPE nanocomposites

195 Figure 3 shows the effect of the PE/AgNPs and PE/FAgNPs nanocomposites on the growth rate
 196 of *E. coli* liquid cultures. It shows that the growth rates of the pure cultures and mixed cultures with
 197 PE slow down after 4h of cultivation. The log phases of the pure cultures and mixed cultures with
 198 neat PE are about 93% after 1h cultivation, whereas they are 85 % in the case of mixed cultures with
 199 PE/AgNPs. Thus, the *E. coli* bacterial growth is inhibited by the presence of PE/AgNPs
 200 nanocomposites. PE/FeAgNP growth rates of the culture were 81 % after 4h. The presence of
 201 FeAgNPs in the PE matrix exhibits a higher antibacterial activity, as compared to the AgNPs. The
 202 FeAgNPs had showed a higher bactericidal activity against staphylococcus aureus bacteria compared
 203 to AgNPs 28 due to: i) a high catalytic activity of AgNPs dispersion and stability due to the Fe₃O₄
 204 carrier, and ii) a large surface contact area between the bacterial cell membrane and the hybrid
 205 nanoparticles.



206
 207 *Figure 3.* Growth rate of *E. coli* liquid cultures of neat PE and nanocomposites with AgNPs and hybrid
 208 FeAgNPs. The data shown represent the average of three cultures (standard deviation < 2 %).

209 Since the average size of AgNPs in FeAgNPs was bigger than that of AgNPs, the above findings
 210 may be due to the faster Ag⁺ release rate from the Fe₃O₄-Ag hybrid nanoparticles. It was suggested
 211 that the ionization of AgNPs in hybrid nanostructure was accelerated by Fe³⁺ ions. It has reported
 212 that addition of Ag and Fe³⁺ enhances the bio-leaching efficiency of the As-bearing gold ore and the
 213 electron transfer from Ag-core to the FeCo shell in 15 nm hybrid nanoparticles which are proven by
 214 XPS results⁴⁵.



215

216

217

Figure 4. Mechanism of inactivation of *E. coli* by FeAgNPs in which the electron exchange between AgNPs and FeNPs promotes the formation of the Ag^+ -ion leading to inactivation of *E. coli*.

218

219

220

221

222

223

224

225

226

It is widely accepted that nano-silver interacts with bacterial membranes and causes cell wall disruption.⁴⁶⁻⁴⁷ The AgNPs absorbed on the outer bacteria membrane surface penetrates into the cytoplasm and inhibits cell replication⁴⁸. The AgNPs simultaneously induce apoptosis and inhibit DNA synthesis due to the silver ions (Ag^+)⁴⁹. Oxidation/reduction of silver ions and Fe^+ promoting the release of silver ions to kill bacteria would proceed. In a reversible process, the concentration of silver ions remained stable in hybrid nanoparticles showing a higher antibacterial activity compared to AgNPs. Based on the results mentioned above, we suggest a novel mechanism of the inactivation of bacteria by FeAgNPs hybrids. The Ag^+ would intervene in a reversible electron transfer to Fe^{3+} (Fig. 4).

227

3.3. Nanoscale architecture of PE /FeAgNPs nanocomposites

228

229

230

231

232

233

234

235

236

237

238

239

240

241

242

243

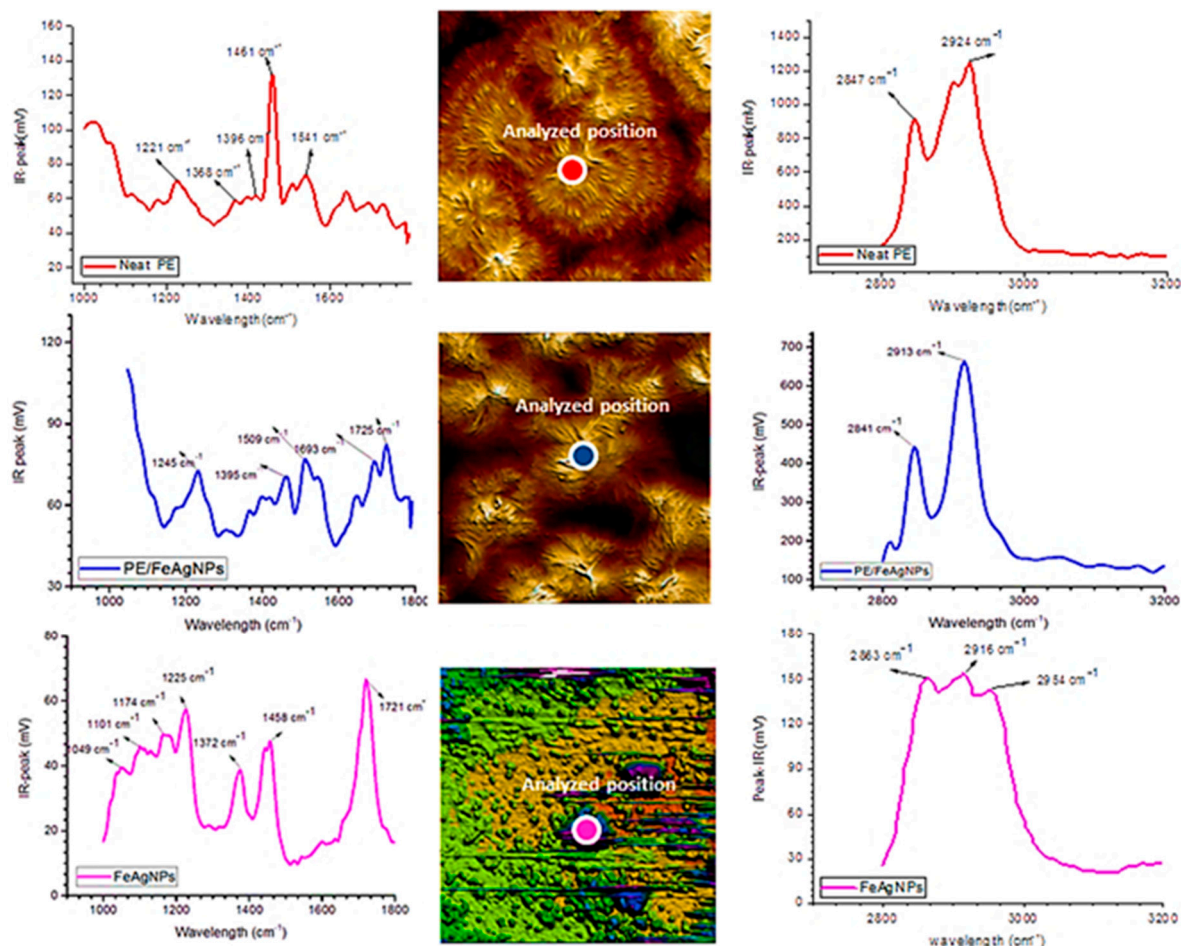
244

245

246

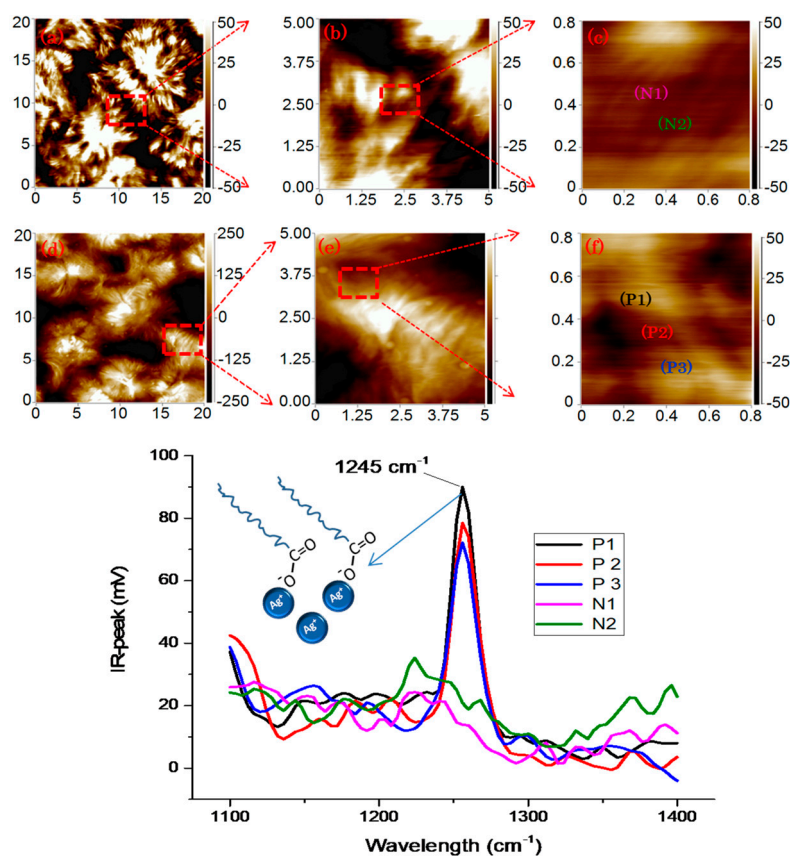
Figure 5 shows the morphology of the PE/FeAgNPs of neat PE and PE/FeAgNPs nanocomposites. The nanocomposites present a very different structure compared to that of neat PE in which the PE exhibits banded spherulites with sizes from 10-20 μm . The formation of ring-banded spherulites of semi-crystalline polymers is well known. The concerted twisting of the crystallographic orientation takes place during lamella growth under effect of surface stress but the arrangement of lamella in the banded spherulites is still an open question. It has been suggested that lamella stacks were continuously twisted up and down to create of ridge and valley banded spherulites, respectively. The valley areas are basically composed by plat-on lamella while the edge-on lamellas are present in ridge areas. However, this band structure is not observed in the case of PE/FeAgNPs nanocomposites. This can be attributed to nanoparticles acting as a nucleation agent for the crystallization at an early stage of the crystallization. This can explain why the nanocomposites possess a higher spherulite density with smaller sizes compared to those of neat PE. It is interesting that the PE/FeAgNPs structure of spherulites was mainly composed by edge on lamella with a growth direction perpendicular to the substrate. This structure gives a more suitable configuration for the release of nanoparticles during the antibacterial tests. The IR spectra in Figure 5 (left and right sides) show that the main vibrational peaks appearing in the IR spectra of neat PE are similar to those measured by the traditional FT-IR microscope related to the intensity and position. The bands at 2924 and 2874 cm^{-1} are assigned to the vibration of symmetric and asymmetric methylene groups. These bands shift to lower frequencies in the case of nanocomposites due to the contribution of long alkyl

247 chain of oleic acid and oleylamine of the nanoparticles coating. The vibrational bands at 1461, 1396
 248 and 1368 cm^{-1} , assigned to CH_2 bending, CH_3 bending and CH_2 wagging, respectively, shift to lower
 249 frequencies in the nanocomposites. Particularly, a new peak at about 1245 cm^{-1} is observed in the case of
 250 nanocomposites which is slightly different to that observed in the case of pure nanoparticles at
 251 about 1225 cm^{-1} . This band is probably due to the presence of C-O stretching in the ester and H
 252 bonded hydroxyl group stretching.⁵⁰ The appearance of the peak at 1245 cm^{-1} is important to identify
 253 the presence of nanoparticles near the sample surface of the nanocomposites and it can be used as a
 254 marker to detect nanocomposites in PE matrix.



255
 256 **Figure 5.** Nano-IR spectra of neat PE, PE/FeAgNPs nanocomposites and pure dumbbell like-FeAgNPs.
 257 The middle column shows AFM images at the position at which the IR spectra were analyzed. Sample
 258 thicknesses were about 500 nm and films were deposited on gold substrates.

259 Figure 6 shows high-resolution AFM images of neat PE and the surface nanocomposites. The
 260 morphology of the spherulites is shown in Figure 5, but not the contour of the nanoparticle surface.
 261 The presence of nanoparticles on the sample was therefore determined by IR-spectroscopy. The peak
 262 at 1245 cm^{-1} was assigned to the C-O stretching in the OL/OLA layer (P1-P3), but it is absent in neat
 263 PE as shown in Figure 7. The distribution of nanoparticles was obtained by TEM.



264

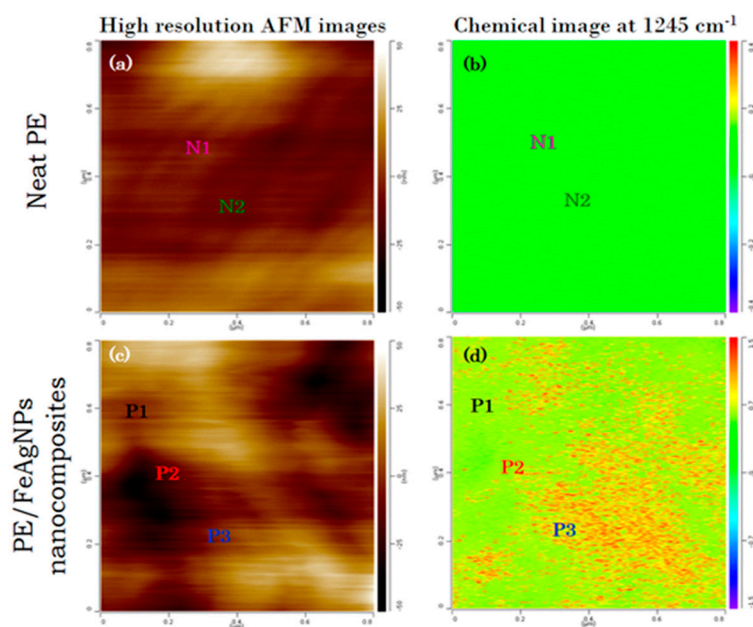
265

266

267

268

Figure 6. High-resolution AFM images of neat PE at different magnifications (a, b, c); high-resolution AFM images of morphology of PE/FeAgNPs nanocomposites (d, e, f) and IR spectra (Figure 6g) of neat PE at position N1 and N2, the spectra of PE/FeAgNPs nanocomposites at different positions P1, P2, P3.



269

270

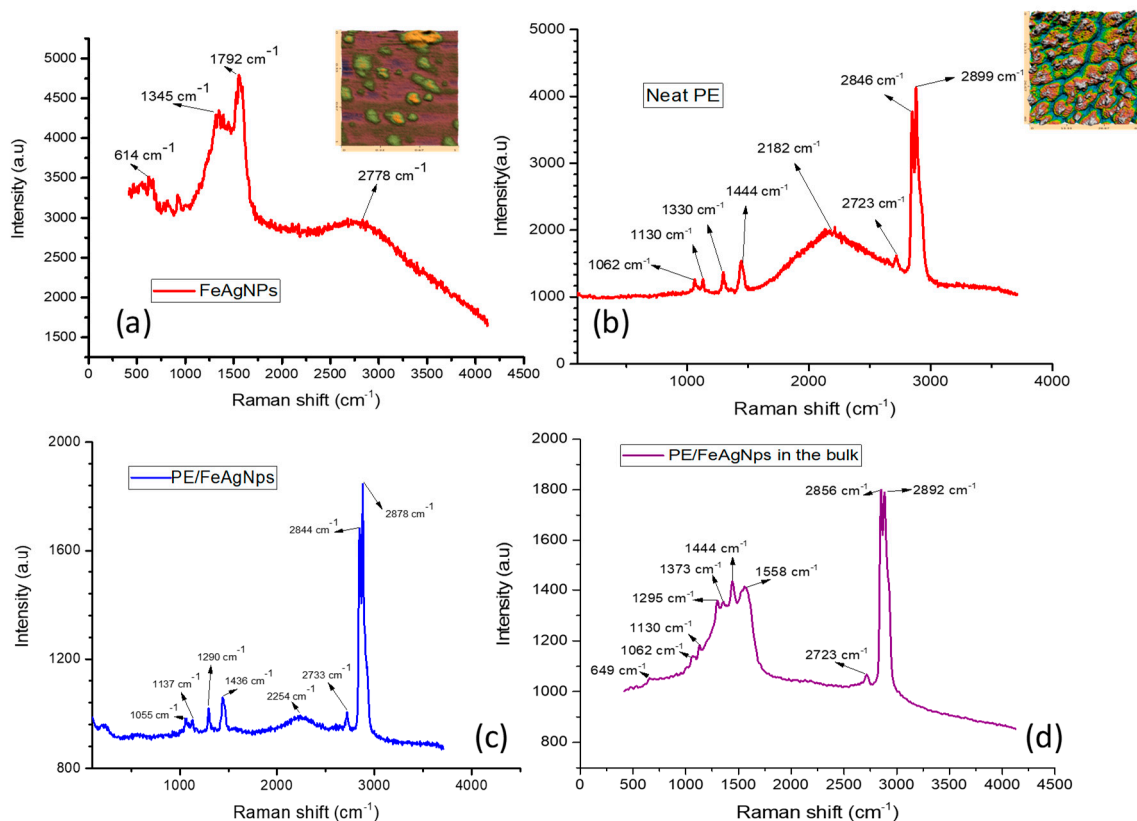
271

272

273

Figure 7. a) high resolution AFM images of neat PE; b) IR-mapping image of neat PE; c) high resolution AFM images of PE/FeAgNPs nanocomposites; d) IR mapping image of PE/FeAgNPs nanocomposites. The points N1, N2, P1, P2, P3 are points corresponding to the nano-spectra analysis described below in Figure 8 c, f. Film thickness was close to 500 nm, deposited on Si-wafer substrate.

274 Resonance enhanced IR-spectroscopy single beam mode was used to obtain a dimensional
 275 mapping image of C-O stretching at 1245 cm^{-1} in the area shown in Figure 7. In the case of neat PE,
 276 IR- absorption mapping at 1245 cm^{-1} was observed to be negligible. The band was absent in neat PE
 277 shown in Figures 6c and 6g. However, for the PE/FeAgNPs nanocomposites, the absorption of C-O
 278 stretching was observed. In fact, there are some domains in which, the IR-absorption of C-O was
 279 strong. This high vibrational absorption was due to the presence of OL/OLA on the surface of hybrid
 280 nanoparticles. For the first time nanoparticles are detected on a polymer matrix in the nanoscale
 281 without using of TEM technique. This is a non-destructive method for the characterization of
 282 nanoparticles dispersed on a polymer matrix.



283
 284 **Figure 8.** Raman spectra of neat PE, FeAgNPs and PE/FeAgNPs, nanocomposites with high-resolution
 285 AFM images. Right hand images show the position of FeAgNPs together with the spectra of neat PE,
 286 PE/FeAgNPs and PE/FeAgNPs nanocomposites. Nano-Raman spectra are shown on the left-hand
 287 side.

288 Figure 8 shows the AFM-Raman spectra and AFM images with the characteristic bands for
 289 FeAgNPs located at 1792 , 1345 and 614 cm^{-1} . It is interesting to see that the typical Raman shift of
 290 magnetite Fe_3O_4 around 668 - 670 cm^{-1} was not observed in both FeAgNPs and nanocomposites.⁵¹
 291 However, two new bands at 613 and 1345 cm^{-1} appeared and were assigned to the Raman vibrational
 292 peaks of $\alpha\text{-Fe}_2\text{O}_3$.⁵² These bands were visible on FeAgNPs alone and in the nanocomposite films. This
 293 may involve the phase transformation from Fe_3O_4 to $\alpha\text{-Fe}_2\text{O}_3$ hexagonal plates. In other words, the
 294 electron transfer from AgNPs to Fe_3O_4 leads to the reduction from Fe^{3+} to Fe^{2+} ions during the
 295 nucleation/growth of Fe_3O_4 polyhedral particles as described above in Figure 4. The broadening of
 296 the peak at 1792 and 2778 cm^{-1} is due to the vibrational of carbonyl group and methylene group in
 297 the structure of oleic acid⁵³. In neat PE, characteristic Raman vibrational bands are seen at 1060 and
 298 1130 cm^{-1} and both are assigned to C-C stretching; the bands at 1295 , 1444 , 2846 , 2899 cm^{-1} are assigned
 299 to methylene twisting, CH_2 wagging and asymmetric and symmetric CH_2 stretching vibrations. The
 300 shift to lower frequencies is due to the change in the crystallinity and of the lamella assembly on the

301 PE-surface. Two new bands observed at 1558 and 1373 cm^{-1} in the Raman spectrogram of the
302 PE/FeAgNPs particles, but could not be assigned at the present time.

303 4. Conclusions

304 This study presents the synthesis of new and uniform hybrid nanoparticles nano-spheres of
305 AgNPs (6-8 nm) and dumbbell like-hybrid FeAgNPs (15-16 nm). The activity was evaluated when
306 they are incorporated a polyolefin. By resonance enhanced atomic force microscopy coupled infrared
307 spectroscopy (nano-IR), it was possible to detect and identify the distribution of the nanoparticles in
308 the polymer matrix. The lamella assembly and the spherulite structure of PE/FeAgNPs are also
309 examined. AFM-Raman spectra of the nanocomposites provide useful information about electron-
310 transfer mechanism of the hybrid nanoparticles, resulting in a higher antibacterial activity. The
311 electron-transfer would proceed from hybrid FeAgNPs and AgNPs to $\text{Fe}_3\text{O}_4\text{NPs}$ in a reversible
312 fashion. The ionization of AgNPs in hybrid nanostructure might be accelerated by Fe^{3+} ions. The as-
313 prepared nanocomposites exhibit a self-sterilizing property, avoiding the formation of biofilms the
314 most dangerous source able to spread for long times toxic bacteria into the environment.

315 **Author Contributions:** P.N.T and S. R. contributed equally to this work

316 **Funding:** This work was financial supported by Natural Sciences and Engineering Research Council of Canada
317 (NSERC) and the Vietnam Academy of Science and Technology (VAST). This work was also partly supported
318 by NAFOSTED (grant 103.02-2012.74).

319 **Acknowledgments:** We thank Patricia (University of Montreal, Canada) for help with the AFM-IR
320 measurements.

321 **Conflicts of Interest:** The authors declare no conflict of interest

322 References

- 323 1. Wang, L.-S.; Gupta, A.; Rotello, V. M., Nanomaterials for the Treatment of Bacterial Biofilms. *ACS Infectious*
324 *Diseases* **2016**, *2* (1), 3-4.
- 325 2. Pappas, H. C.; Phan, S.; Yoon, S.; Edens, L. E.; Meng, X.; Schanze, K. S.; Whitten, D. G.; Keller, D. J., Self-
326 Sterilizing, Self-Cleaning Mixed Polymeric Multifunctional Antimicrobial Surfaces. *ACS Applied Materials &*
327 *Interfaces* **2015**, *7* (50), 27632-27638.
- 328 3. Hui, L.; Su, Y.; Ye, T.; Liu, Z.; Tian, Q.; He, C.; Zhao, Y.; Chen, P.; Wang, X.; Han, W.; Luo, Y.; Wang, B.,
329 Self-Sterilizing and Regeneratable Microchip for the Precise Capture and Recovery of Viable Circulating Tumor
330 Cells from Patients with Cancer. *ACS Applied Materials & Interfaces* **2018**, *10* (1), 207-218.
- 331 4. Turner, A.; Chen, S.-N.; Joike, M. K.; Pendlan, S. L.; Pauli, G. F.; Farnsworth, N. R., Inhibition of
332 Uropathogenic *Escherichia coli* by Cranberry Juice: A New Antiadherence Assay. *Journal of Agricultural and Food*
333 *Chemistry* **2005**, *53* (23), 8940-8947.
- 334 5. Osawa, R.; Kamide, T.; Satoh, Y.; Kawano, Y.; Ohtsu, I.; Dairi, T., Heterologous and High Production of
335 Ergothioneine in *Escherichia coli*. *Journal of Agricultural and Food Chemistry* **2018**, *66* (5), 1191-1196.
- 336 6. Xiu, Z.-m.; Zhang, Q.-b.; Puppala, H. L.; Colvin, V. L.; Alvarez, P. J. J., Negligible Particle-Specific
337 Antibacterial Activity of Silver Nanoparticles. *Nano Letters* **2012**, *12* (8), 4271-4275.
- 338 7. López-Esparza, J.; Espinosa-Cristóbal, L. F.; Donohue-Cornejo, A.; Reyes-López, S. Y., Antimicrobial
339 Activity of Silver Nanoparticles in Polycaprolactone Nanofibers against Gram-Positive and Gram-Negative
340 Bacteria. *Industrial & Engineering Chemistry Research* **2016**, *55* (49), 12532-12538.
- 341 8. Ramalingam, B.; Parandhaman, T.; Das, S. K., Antibacterial Effects of Biosynthesized Silver Nanoparticles
342 on Surface Ultrastructure and Nanomechanical Properties of Gram-Negative Bacteria viz. *Escherichia coli* and
343 *Pseudomonas aeruginosa*. *ACS Applied Materials & Interfaces* **2016**, *8* (7), 4963-4976.

- 344 9. Taglietti, A.; Diaz Fernandez, Y. A.; Amato, E.; Cucca, L.; Dacarro, G.; Grisoli, P.; Necchi, V.; Pallavicini, P.;
345 Pasotti, L.; Patrini, M., Antibacterial Activity of Glutathione-Coated Silver Nanoparticles against Gram Positive
346 and Gram Negative Bacteria. *Langmuir* **2012**, *28* (21), 8140-8148.
- 347 10. Tang, D.; Yuan, R.; Chai, Y., Magnetic Core-Shell Fe₃O₄@Ag Nanoparticles Coated Carbon Paste Interface
348 for Studies of Carcinoembryonic Antigen in Clinical Immunoassay. *The Journal of Physical Chemistry B* **2006**, *110*
349 (24), 11640-11646.
- 350 11. Liu, C. H.; Zhou, Z. D.; Yu, X.; Lv, B. Q.; Mao, J. F.; Xiao, D., Preparation and characterization of Fe₃O₄/Ag
351 composite magnetic nanoparticles. *Inorganic Materials* **2008**, *44* (3), 291-295.
- 352 12. Chang, M.; Lin, W.-S.; Xiao, W.; Chen, Y.-N., Antibacterial Effects of Magnetically-Controlled Ag/Fe₃O₄
353 Nanoparticles. *Materials* **2018**, *11* (5).
- 354 13. Liu, X.; Yin, G.; Yi, Z.; Duan, T., Silk Fiber as the Support and Reductant for the Facile Synthesis of Ag-
355 Fe₃O₄ Nanocomposites and Its Antibacterial Properties. *Materials* **2016**, *9* (7).
- 356 14. Nguyen-Tri, P.; Nguyen, T. A.; Carriere, P.; Ngo Xuan, C., Nanocomposite Coatings: Preparation,
357 Characterization, Properties, and Applications. *International Journal of Corrosion* **2018**, *2018*, 1-19.
- 358 15. Pyun, J.; Jia, S.; Kowalewski, T.; Patterson, G. D.; Matyjaszewski, K., Synthesis and Characterization of
359 Organic/Inorganic Hybrid Nanoparticles: Kinetics of Surface-Initiated Atom Transfer Radical Polymerization
360 and Morphology of Hybrid Nanoparticle Ultrathin Films. *Macromolecules* **2003**, *36* (14), 5094-5104.
- 361 16. Li, X.; Ji, N.; Li, M.; Zhang, S.; Xiong, L.; Sun, Q., Morphology and Structural Properties of Novel Short
362 Linear Glucan/Protein Hybrid Nanoparticles and Their Influence on the Rheological Properties of Starch Gel.
363 *Journal of Agricultural and Food Chemistry* **2017**, *65* (36), 7955-7965.
- 364 17. Nguyen Tri, P.; Guinault, A.; Sollogoub, C., Élaboration et propriétés des composites polypropylène
365 recyclé/fibres de bambou. *Matériaux & Techniques* **2012**, *100* (5), 413-423.
- 366 18. Azizi, S.; David, E.; Fréchette, M. F.; Nguyen-Tri, P.; Ouellet-Plamondon, C. M., Electrical and thermal
367 conductivity of ethylene vinyl acetate composite with graphene and carbon black filler. *Polymer Testing* **2018**, *72*,
368 24-31.
- 369 19. Azizi, S.; David, E.; Fréchette, M. F.; Nguyen-Tri, P.; Ouellet-Plamondon, C. M., Electrical and thermal
370 phenomena in low-density polyethylene/carbon black composites near the percolation threshold. *Journal of*
371 *Applied Polymer Science* **2018**, 47043.
- 372 20. Boukehili, H.; Nguyen-Tri, P., Helium gas barrier and water absorption behavior of bamboo fiber
373 reinforced recycled polypropylene. *Journal of Reinforced Plastics and Composites* **2012**, *31* (23), 1638-1651.
- 374 21. Nguyen Tri, P.; Gilbert, V., Non-isothermal Crystallization Kinetics of Short Bamboo Fiber-reinforced
375 Recycled Polypropylene Composites. *Journal of Reinforced Plastics and Composites* **2010**, *29* (17), 2576-2591.
- 376 22. Nguyen Tri, P.; Sollogoub, C.; Guinault, A., Relationship between fiber chemical treatment and properties
377 of recycled pp/bamboo fiber composites. *Journal of Reinforced Plastics and Composites* **2010**, *29* (21), 3244-3256.
- 378 23. Nguyen Tri, P.; Nguyen, T. A.; Nguyen, T. H.; Carriere, P., Antibacterial Behavior of Hybrid Nanoparticles.
379 **2019**, 141-155.
- 380 24. Tri, P. N.; Rtimi, S.; Nguyen, T. A.; Vu, M. T., Physics, Electrochemistry, Photochemistry, and
381 Photoelectrochemistry of Hybrid Nanoparticles. **2019**, 95-123.
- 382 25. Nguyen Tri, P.; Ouellet-Plamondon, C.; Rtimi, S.; Assadi, A. A.; Nguyen, T. A., Methods for Synthesis of
383 Hybrid Nanoparticles. **2019**, 51-63.
- 384 26. Nguyen, T. V.; Nguyen Tri, P.; Nguyen, T. D.; El Aidani, R.; Trinh, V. T.; Decker, C., Accelerated
385 degradation of water borne acrylic nanocomposites used in outdoor protective coatings. *Polymer Degradation and*
386 *Stability* **2016**, *128*, 65-76.

- 387 27. Nguyen Tri, P.; Prud'homme, R. E., Crystallization and Segregation Behavior at the Submicrometer Scale
388 of PCL/PEG Blends. *Macromolecules* **2018**, *51* (18), 7266-7273.
- 389 28. Nguyen, T. P., Nanoscale analysis of the photodegradation of Polyester fibers by AFM-IR *Journal of*
390 *Photochemistry and Photobiology A: Chemistry* **2018**, *Accepted*.
- 391 29. Tri, P. N.; Prud'homme, R. E., Nanoscale Lamellar Assembly and Segregation Mechanism of Poly(3-
392 hydroxybutyrate)/Poly(ethylene glycol) Blends. *Macromolecules* **2018**, *51* (1), 181-188.
- 393 30. Satyabrata, M. T., Anh Nguyen; Phuong, Nguyen-Tri, *Noble Metal-Metal Oxide Hybrid Nanoparticles*.
394 Elsevier: 2018; Vol. 1.
- 395 31. El Aidani, R.; Nguyen-Tri, P.; Malajati, Y.; Lara, J.; Vu-Khanh, T., Photochemical aging of an e-
396 PTFE/NOMEX® membrane used in firefighter protective clothing. *Polymer Degradation and Stability* **2013**, *98* (7),
397 1300-1310.
- 398 32. Zeb, G.; Tri, P. N.; Palacin, S.; Le, X. T., Pulse potential deposition of thick polyvinylpyridine-like film on
399 the surface of titanium nitride. *RSC Adv.* **2016**, *6* (84), 80825-80829.
- 400 33. Nguyen, T. V.; Le, X. H.; Dao, P. H.; Decker, C.; Nguyen-Tri, P., Stability of acrylic polyurethane coatings
401 under accelerated aging tests and natural outdoor exposure: The critical role of the used photo-stabilizers.
402 *Progress in Organic Coatings* **2018**, *124*, 137-146.
- 403 34. Cowcher, D. P.; Deckert-Gaudig, T.; Brewster, V. L.; Ashton, L.; Deckert, V.; Goodacre, R., Detection of
404 Protein Glycosylation Using Tip-Enhanced Raman Scattering. *Analytical Chemistry* **2016**, *88* (4), 2105-2112.
- 405 35. Huang, S.; Pandey, R.; Barman, I.; Kong, J.; Dresselhaus, M., Raman Enhancement of Blood Constituent
406 Proteins Using Graphene. *ACS Photonics* **2018**, *5* (8), 2978-2982.
- 407 36. Dazzi, A.; Prater, C. B., AFM-IR: Technology and Applications in Nanoscale Infrared Spectroscopy and
408 Chemical Imaging. *Chemical Reviews* **2017**, *117* (7), 5146-5173.
- 409 37. Hartman, T.; Wondergem, C. S.; Kumar, N.; van den Berg, A.; Weckhuysen, B. M., Surface- and Tip-
410 Enhanced Raman Spectroscopy in Catalysis. *The Journal of Physical Chemistry Letters* **2016**, *7* (8), 1570-1584.
- 411 38. Koutzarova, T.; Kolev, S.; Ghelev, C.; Paneva, D.; Nedkov, I., Microstructural study and size control of iron
412 oxide nanoparticles produced by microemulsion technique. *physica status solidi (c)* **2006**, *3* (5), 1302-1307.
- 413 39. Rahman, O. u.; Mohapatra, S. C.; Ahmad, S., Fe₃O₄ inverse spinal super paramagnetic nanoparticles.
414 *Materials Chemistry and Physics* **2012**, *132* (1), 196-202.
- 415 40. Kuriakose, S.; Choudhary, V.; Satpati, B.; Mohapatra, S., Enhanced photocatalytic activity of Ag-ZnO
416 hybrid plasmonic nanostructures prepared by a facile wet chemical method. *Beilstein J Nanotechnol* **2014**, *5*, 639-
417 50.
- 418 41. Mandal, S.; Wang, J.; Winans, R. E.; Jensen, L.; Sen, A., Quantum Size Effects in the Optical Properties of
419 Ligand Stabilized Aluminum Nanoclusters. *The Journal of Physical Chemistry C* **2013**, *117* (13), 6741-6746.
- 420 42. Peng, S.; McMahon, J. M.; Schatz, G. C.; Gray, S. K.; Sun, Y., Reversing the size-dependence of surface
421 plasmon resonances. *Proceedings of the National Academy of Sciences* **2010**, *107* (33), 14530-14534.
- 422 43. Xu, S.; Hartvickson, S.; Zhao, J. X., Engineering of SiO₂-Au-SiO₂ Sandwich Nanoaggregates Using a
423 Building Block: Single, Double, and Triple Cores for Enhancement of Near Infrared Fluorescence. *Langmuir* **2008**,
424 *24* (14), 7492-7499.
- 425 44. Siiman, O.; Bumm, L. A.; Callaghan, R.; Blatchford, C. G.; Kerker, M., Surface-enhanced Raman scattering
426 by citrate on colloidal silver. *The Journal of Physical Chemistry* **1983**, *87* (6), 1014-1023.
- 427 45. Chudasama, B.; Vala, A. K.; Andhariya, N.; Upadhyay, R. V.; Mehta, R. V., Enhanced antibacterial activity
428 of bifunctional Fe₃O₄-Ag core-shell nanostructures. *Nano Research* **2009**, *2* (12), 955-965.

- 429 46. Buszewski, B.; Railean-Plugaru, V.; Pomastowski, P.; Rafinska, K.; Szultka-Mlynska, M.; Golinska, P.;
430 Wypij, M.; Laskowski, D.; Dahm, H., Antimicrobial activity of biosilver nanoparticles produced by a novel
431 *Streptacidiphilus durhamensis* strain. *J Microbiol Immunol Infect* **2018**, *51* (1), 45-54.
- 432 47. Banach, M.; Tymczyna, L.; Chmielowiec-Korzeniowska, A.; Pulit-Prociak, J., Nanosilver Biocidal Properties
433 and Their Application in Disinfection of Hatchers in Poultry Processing Plants. *Bioinorg Chem Appl* **2016**, *2016*,
434 5214783.
- 435 48. Bao, H.; Yu, X.; Xu, C.; Li, X.; Li, Z.; Wei, D.; Liu, Y., New toxicity mechanism of silver nanoparticles:
436 promoting apoptosis and inhibiting proliferation. *PLoS One* **2015**, *10* (3), e0122535.
- 437 49. Wakshlak, R. B.; Pedahzur, R.; Avnir, D., Antibacterial activity of silver-killed bacteria: the "zombies" effect.
438 *Sci Rep* **2015**, *5*, 9555.
- 439 50. Žagar, E.; Grdadolnik, J., An infrared spectroscopic study of H-bond network in hyperbranched polyester
440 polyol. *Journal of Molecular Structure* **2003**, *658* (3), 143-152.
- 441 51. Lu, J. F.; Tsai, C. J., Hydrothermal phase transformation of hematite to magnetite. *Nanoscale Res Lett* **2014**, *9*
442 (1), 230.
- 443 52. Bellot-Gurlet, L.; Neff, D.; Réguer, S.; Monnier, J.; Saheb, M.; Dillmann, P., Raman Studies of Corrosion
444 Layers Formed on Archaeological Irons in Various Media. *Journal of Nano Research* **2009**, *8*, 147-156.
- 445 53. Schie, I. W.; Nolte, L.; Pedersen, T. L.; Smith, Z.; Wu, J.; Yahiatene, I.; Newman, J. W.; Huser, T., Direct
446 comparison of fatty acid ratios in single cellular lipid droplets as determined by comparative Raman
447 spectroscopy and gas chromatography. *Analyst* **2013**, *138* (21), 6662-70.